Tuning the hydrogen storage properties of Ti-V-Nb-Cr alloys by controlling the Cr/(TiVNb) ratio

R.B. Strozi, B.H. Silva, D.R. Leiva, C. Zlotea, W.J. Botta, G. Zepon

R.B. Strozi, B.H. Silva, D.R. Leiva, C. Zlotea, W.J. Botta, et al.. Tuning the hydrogen storage properties of Ti-V-Nb-Cr alloys by controlling the Cr/(TiVNb) ratio. Journal of Alloys and Compounds, 2023, 932, pp.167609. 10.1016/j.jallcom.2022.167609 . hal-04155852

Tuning the hydrogen storage properties of Ti-V-Nb-Cr alloys by controlling the Cr/(TiVNb) ratio

R.B. Strozi[1,2,#], B.H. Silva[3], D.R. Leiva[2], C. Zlotea[1], W.J. Botta[2], G. Zepon[2]

[1]University Paris Est Créteil, CNRS, ICMPE, UMR 7182, 2 rue Henri Dunant, 94320 Thiais, France

[2]Department of Materials Engineering, Federal University of São Carlos, DEMa-UFSCar, 13565-905, São Carlos, Brazil

[3]Graduate Program in Materials Science and Engineering, Federal University of São Carlos, PPGCEM-UFSCar, 13565-905, São Carlos, Brazil

#corresponding author: renato.belli-strozi@cnrs.fr

Abstract

This work presents an effective way to tune the thermodynamic properties of hydrogen absorption/desorption of body-centered multicomponent alloys (BCC-MCAs). A two-fold computational design was applied to screen the $(TiVNb)_{100-x}Cr_x$ system. First, the calculation of phase diagrams (CALPHAD) approach was used, aiming to BCC alloys. Secondly, thermodynamic modeling was employed to predict the thermodynamics of the metal-hydrogen systems. $(TiVNb)_{100-x}Cr_x$ alloys with x = 30, 35 and 40 alloys were produced by arc-melting. The $(TiVNb)_{70}Cr_{30}$ and $(TiVNb)_{65}Cr_{35}$ alloys crystallize as a major BCC phase, while the $(TiVNb)_{60}Cr_{40}$ is composed mainly of a C15 Laves-type phase. The CALPHAD approach well predicted this tendency. The BCC $(TiVNb)_{70}Cr_{30}$ and $(TiVNb)_{65}Cr_{35}$ alloys absorb a large amount of hydrogen up to 2 H/M forming a dihydride. On the contrary, the $(TiVNb)_{60}Cr_{40}$ alloy displays a reduced capacity due to the low hydrogen uptake of the C15 phase. The thermodynamics of hydrogen absorption/desorption of BCC-MCAs was experimentally investigated via the acquisition of pressure-composition-temperature (PCT) diagrams. The experimental values are in good agreement with the modeling, confirming the accuracy of the computational approach.

Moreover, it was demonstrated that increasing Cr content up to 35 % significantly impacts the thermodynamic properties, enabling reversible hydrogen absorption/desorption (for H/M ≈ 1) at room temperature.

Keywords: Metal hydrides; Hydrogen as an energy carrier; Multicomponent BCC alloys; Thermodynamic stability.

1. Introduction

Although fossil energy sources are helpful to enable a comfortable lifestyle for humanity, the counterpoint is the greenhouse gas emissions causing climate change. The use of green hydrogen as an energy carrier emerges as an alternative to replace the current energy matrix. The hydrogen produced via renewable and clean energy sources can be helpful to mitigate the effects of climate change. However, technologies for safe and efficient hydrogen storage are still lacking. Suitable operating conditions for various applications can be achieved by using metal hydrides (MHs) as a hydrogen vector, being an alternative to traditional gas and liquid storage methods [1]. MH properties depend on both chemical composition and structure, and to overcome the remaining technological challenges, they have been extensively studied. In this regard, the advent of the MCAs brought new perspectives. The conception of MCAs derivates from the high entropy alloys (HEA). The most common HEA definition states that they have at least five alloying elements with concentrations between 5 and 35 at.% [2]. The multicomponent character contributes to increasing the alloy's configurational entropy of mixing. From a thermodynamic point of view, the high entropy would be high enough to result in stable single-phase solid solutions at high temperatures. The multicomponent character of HEAs has stimulated new ideas since the broad compositional range of multicomponent systems can provide a fine-tuning of MH properties for different applications [3].

The earliest investigations of MCA metal hydrides report the study of ordered C14 Laves-type structure ($MgZn_2$ type, P63/mmc space group) multicomponent alloys [4]. The hydrogen storage behavior of these alloys has been studied via electrochemical and gas-solid reactions and attractive hydrogen properties such as good cyclability and mild operation conditions can be achieved [5–9]. Another prominent group of MCAs for hydrogen storage is based on body-centered cubic solid solutions (BCC) [10–12]. These BCC metal hydrides can achieve a hydrogen-to-metal ratio (H/M) of about 2 at room temperature and the hydrogenation usually occurs in a two-stage absorption reaction. For instance, by in-situ Synchrotron X-ray diffraction, Zlotea *et al.* demonstrated that the TiZrNbHfTa equiatomic alloy crystallizes as a BCC-type structure (W-type, Im-3m, 229) and can absorb and desorb hydrogen in a reversible two-step process [13]. Upon absorption, the dilute hydrogen BCC solid solution phase (α-phase) undergoes a phase change by forming an intermediate monohydride (β-phase), followed by the formation of an FCC phase (δ-phase, with CaF_2-type structure) with H/M ≈ 2. The thermodynamics of metal-hydrogen systems can be experimentally assessed by acquiring PCT diagrams. For hydrogenation of BCC alloys under isothermal conditions, a low equilibrium plateau pressure is associated with the $\alpha \rightarrow \beta$ phase transformation, followed by a higher plateau pressure for the $\beta \rightarrow \delta$ transformation.

BCC-MCAs are commonly composed of refractory elements with high hydrogen affinity. Consequently, they have very low equilibrium plateau pressure and very high decomposition temperatures. The stability of MH can be strongly affected by the differences in the chemical composition [14,15]. Significant efforts are being made in developing tools and strategies to assist researchers in exploring the vast compositional field of MCA-MHs [16,17]. An approach to tune MH properties is the addition of non-hydride forming elements into the BCC lattice [18,19]. In previous studies of the $(TiVNb)_{100-x}Cr_x$ system, we demonstrated that the Cr addition in solid solution significantly impacts the thermodynamics properties of the TiVNbCr-H system [20]. Structural characterization indicates that samples with composition range between 15 and 35 at.% Cr crystallizes in a BCC-type structure with a dendritic microstructure. Since Cr is a non-hydride forming element, increasing its concentration has a practical impact of increasing the equilibrium plateau pressure. Based on these previous findings, we propose that the hydrogen storage properties of Ti-V-Nb-Cr alloys can be fine-tuned by controlling the Cr/(TiVNb) ratio. CALPHAD method was employed to investigate the effect of the Cr/(TiVNb) ratio on the equilibrium phases of the system. Moreover, the thermodynamic model reported by Zepon *et al.* was employed to calculate the PCT diagrams of the alloys [19]. It is worth stressing that this model was shown to be effective in determining the equilibrium plateau pressure for the alloys of the Ti-V-Nb-Cr systems, such as $(TiVNb)_{85}Cr_{15}$ and $Ti_{28.1}V_{1.3}Nb_{55.4}Cr_{15}$ [19]. Thus, the present work aims to design alloys with the appropriate Cr/(TiVNb) ratio that allows room-temperature absorption/desorption under moderate pressure and with good reversibility and cyclability. The

$(TiVNb)_{100-x}Cr_x$ alloys with x = 30, 35 and 40 were experimentally investigated and the experimental data correlated with the design approach.

2. Materials and Methods

The CALPHAD method was performed using the Thermo-Calc® software and TCHEA5 database. The $(TiVNb)_{100-x}Cr_x$ (x = 30, 35 and 40) alloys were prepared by arc-melting using an Edmund Bühler GmbH furnace operating under an argon atmosphere previously purified by a Ti getter. High purity metals from Alfa-Aesar, namely, Ti granules (99.99%), V pieces (99.7%), Cr pieces (99.99%) and Nb pieces (99.8%), were used as feedstock material. The ingots were flipped over and re-melted five times to ensure compositional homogeneity.

A scanning electron microscope (SEM) Philips XL-30-FEG coupled with an energy-dispersive X-ray spectroscopy (EDS) detector from Bruker (Nano X-Flash 6|60) was used to investigate the local chemical composition. For SEM-EDS analysis, the ingots were crushed using a stainless-steel mortar and pestle and the powder particles were randomly analyzed. X-Ray Diffraction (XRD) was performed with a D8 Advance Brucker diffractometer using Cu-Kα radiation. For XRD analysis, Rietveld refinement was performed with the GSAS-II software [21]. The background was fitted by using the Chebyschev function with at least 3 coefficients and the pseudo-Voigt powder peak profile function was used to model the peaks. The refined parameters were mainly background, displacement, scale factor, lattice parameter, isotropic micro-strain, and crystallite size. No instrument parameters were refined.

The hydrogen desorption temperature was investigated employing differential scanning calorimetry (DSC) coupled with thermogravimetry analysis (TGA) and quadrupole mass spectrometer (QMS) to keep track of gases released during heating. It was used the Netzsch STA 449C instrument operating under constant argon flow (25 ml/min) and heating rate of 10 K/min up to 973 K. The hydrogen sorption performance was evaluated via gas-solid reaction using a Sievert-type apparatus SETARAM® PCT-Pro volumetric instrument. To avoid the deleterious influence of passivation layers during the first hydrogenation, prior to volumetric measurements the samples were thermally activated at 723 K under a dynamic primary vacuum for 3h. Absorption and desorption PCT's were acquired at 303, 323 and 343 K, applying variable doses of hydrogen.

The kinetic experiments were carried out at room temperature, which is around 298 K. The absorption was carried out under 1.5 MPa of H_2.

3. Results and Discussion

3.1 Thermodynamic calculations

3.1.1 CALPHAD

Fig. 1 presents the (TiVNb)-Cr pseudo-binary phase diagram up to 50 at.% Cr. The thermodynamic calculation suggests that under equilibrium conditions the BCC phase could be formed as a single solid solution phase at high temperatures. With 0 at.% Cr, the single BCC phase is stable from the solidus temperature down to 750 K. Up to around 15 at.% Cr, the single BCC phase field is still large, from solidus temperature to 1000 K. Below this temperature the single BCC phase decomposes in two different BCC phases. Above 15 at.% Cr, C15-type Laves phase precipitates upon cooling. Increasing the Cr content leads to an increase in the precipitation temperature of the C15-type Laves phase, ranging from 1000 K for 15 at.% Cr to 1530 K for 45 at.% Cr. Under relatively rapid cooling rates, such as those imposed by arc-melting process for small ingots as employed in this work, it is possible to avoid the precipitation of C15-type Laves phase. Indeed, this was observed for the $(TiVNb)_{85}Cr_{15}$ [20,22] and $(TiVNb)_{75}Cr_{25}$ [18,20]. For the $(TiVNb)_{65}Cr_{35}$ alloy reported in [20], small fraction of C15-Laves phase was formed at the interdentric regions due to solute partitioning during solidification. Increasing the Cr content above 35 at.% might lead to an increase in the C15-Laves phase formation during solidification.

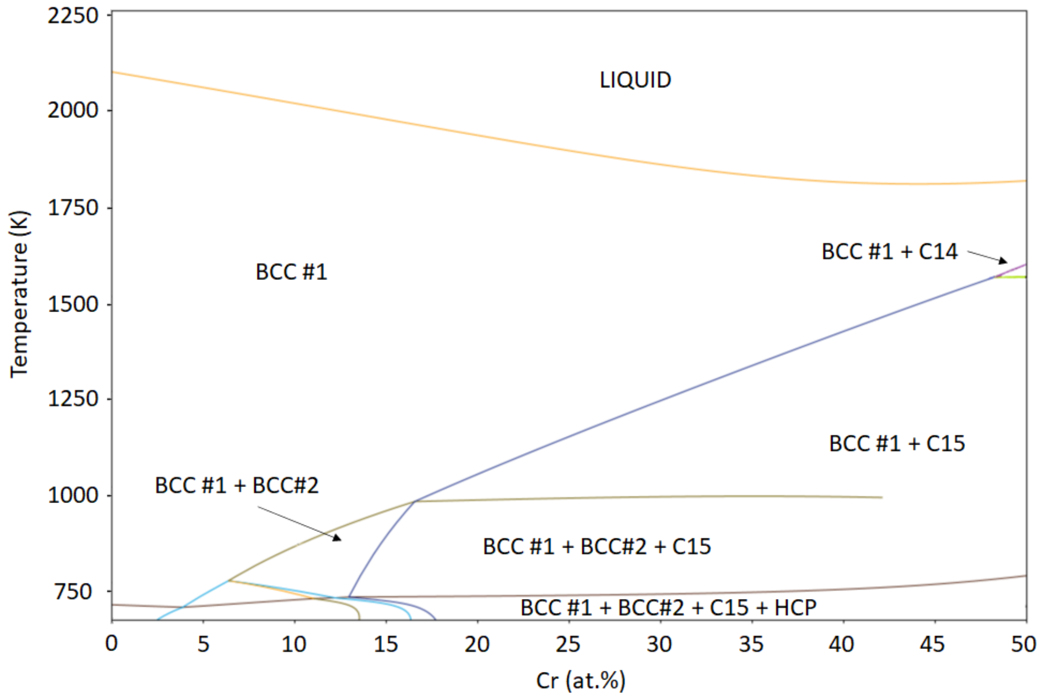

Figure 1: *Pseudo-binary phase diagram calculated by CALPHAD for the* $(TiVNb)_{100-x}Cr_x$ *system. The phase fields are labeled in the figure.*

3.1.2 PCT diagram calculation

Since the CALPHAD calculation and previous investigations demonstrated that the $(TiVNb)_{100-x}Cr_x$ alloy system can form BCC solid solution structure for a wide range of Cr content, one would benefit to know beforehand how the Cr content impacts their hydrogen storage properties. The PCT diagram of an alloy is the key feature that determines their applicability as a hydrogen storage material for a given pressure-temperature condition. For a solid-state hydrogen storage tank operating at room-temperature and mild pressure conditions, the PCT diagram of the alloy needs to have a plateau pressure at room-temperature just above atmospheric pressure, for example, between 0.2 to 1.0 MPa. In this case, it would be possible to load the tank with a relatively low pressure, for instance, 2.0 MPa, which is way below the pressure employed in typical commercial hydrogen gas cylinders (≈ 20 MPa). Moreover, since the plateau pressure is above atmospheric pressure, the hydrogen could be delivered at room-temperature by just releasing the gas of the tank and reducing the system pressure. Slightly increasing the temperature up to 323 K or 343 K, shall increase the equilibrium plateau pressures, which would favor the desorption reaction and likely increase the desorption rate.

Recently, Zepon *et al.* proposed a thermodynamic model to calculate PCT diagrams for multicomponent BCC alloys [19]. In this model, three phases typically observed during the hydrogenation of BCC alloys were considered. The interstitial BCC solid solution (α-phase), the intermediate hydride with either BCC or BCT structure (β-phase), and the FCC hydride (δ-phase). The proposed modeling considers the hydrogen-multicomponent system under the para-equilibrium (PE) condition, in which the metal atoms have low mobility and no long-range diffusion can occur, so there is no change in the composition in terms of metal atoms during hydrogenation [23]. In this case, only hydrogen has enough mobility to change the chemical composition of the phases. The PE is attained when the chemical potential of the metal atoms and hydrogen are the same in all phases in the system. Describing how the Gibbs free energy (ΔG) of each possible phase in the system varies with the hydrogen content is needed to determine their metal and hydrogen chemical potentials. In the model proposed by Zepon *et al.* [19], the authors considered that the enthalpy of a phase (ΔH) varies linearly with hydrogen content. The coefficients of the linear function to describe the ΔH of each possible phase (α, β, and δ) were determined using experimental data of binary hydrides (for α- and β- phases) and total energy calculation by density functional theory (DFT) (only for the δ phase). The authors also considered that the hydrogen partial molar enthalpy of a multicomponent phase was approximated by a mixture rule of the hydrogen partial molar enthalpy of the alloy components having the same structure of the considered phase. The modeling proposed by Garcés *et al.* to describe the interstitial solid solution with site blocking effect (SBE) was used to determine the entropy variation as a function of hydrogen content [24]. A complete description of the calculation method and the advantages and limitations of the model can be found in reference [19]. Moreover, an open-source code to implement the calculations was reported in [25]. Although there are a few limitations on the model's prediction capability, it can be easily employed to investigate the effect of the Cr content on the plateau pressure of the $(TiVNb)_{100-x}Cr_x$ alloys.

Fig. 2(a) presents the calculated PCT curves at 303 K for $(TiVNb)_{100-x}Cr_x$ alloys with Cr content ranging from 10 to 40 at.%. The PCT curves for the $(TiVNb)_{90}Cr_{10}$ and $(TiVNb)_{85}Cr_{15}$ alloys presented two equilibrium plateau pressures. One at low hydrogen concentration and low-pressure levels that indicates the equilibrium between the α-phase and the intermediate hydride (β-phase). Although these equilibrium plateau pressures are very low ($< 10^{-4}$ MPa) and difficult to experimentally be measured, the existence of an equilibrium between a dilute hydrogen BCC solid solution and an intermediate hydride have been confirmed by Silva *et al.* [26] from synchrotron XRD and pair distribution function (PDF) analysis of the $(TiVNb)_{85}Cr_{15}$ alloy. The intermediate hydride in this alloy also has a BCC structure, and the plateau was explained as a hydrogen miscibility gap in the BCC phase. At high hydrogen concentration and high-pressure levels, these alloys present a second equilibrium plateau pressure where the β-phase is in equilibrium with the FCC hydride (δ-phase). The $(TiVNb)_{100-x}Cr_x$ alloys with x from 20 to 40 presented only one equilibrium plateau pressure between the dilute BCC α-phase and the concentrated FCC δ-phase. For these alloys, the plateau width was quite large, which would indicate a high reversible storage capacity, although the plateau widths are not well described yet by the employed thermodynamic model. Thus, we will focus our analysis on the equilibrium plateau pressures, which was proven to be well described by the model. Fig. 2(a) shows that increasing the Cr content from 10 to 40 at.% increases the equilibrium plateau pressure from 10^{-5} MPa to almost 10^{1} MPa. It is worth stressing that only the second plateau pressure between β-phase and δ-phase will be considered for the $(TiVNb)_{90}Cr_{10}$ and $(TiVNb)_{85}Cr_{15}$ alloys. Therefore, the thermodynamic calculation shows that we can finely tune the equilibrium plateau pressure of the $(TiVNb)_{100-x}Cr_x$ alloys by controlling the Cr/(TiVNb) ratio. At 303 K, only the $(TiVNb)_{65}Cr_{35}$ and $(TiVNb)_{60}Cr_{40}$ present equilibrium plateau pressure above 0.1 MPa, 0.44 MPa and 4.71 MPa, respectively. Therefore, these alloys are more likely to present good reversibility at room temperature. The $(TiVNb)_{70}Cr_{30}$ alloy presents a calculated plateau pressure of 0.04 MPa, i.e., near the atmospheric pressure, which could also lead to reasonable reversibility at room temperature. Fig. 2(b) presents the equilibrium plateau pressures of the $(TiVNb)_{100-x}Cr_x$ alloys at 303 K, 323 K and 343 K. One can see that at 343 K, the equilibrium plateau pressure of the $(TiVNb)_{70}Cr_{30}$ is 0.47 MPa, suggesting that the reversibility of this alloy could be favored by a slight increase in temperature. For the $(TiVNb)_{65}Cr_{35}$ and $(TiVNb)_{60}Cr_{40}$, the equilibrium plateau pressure at 343 K are 3.78 MPa and 30.03 MPa, respectively, which could favor the reversibility and potentially increase the desorption rate due to the high driving force for desorption at low pressure. On the other hand, the calculated equilibrium plateau pressure for the $(TiVNb)_{90}Cr_{10}$, $(TiVNb)_{85}Cr_{15}$, $(TiVNb)_{80}Cr_{20}$, and $(TiVNb)_{75}Cr_{25}$ alloys were below 0.1 MPa even at 343 K. Therefore, the thermodynamic calculation indicates that the hydrides of these alloys are quite stable at room-temperature and high temperatures are needed for desorption. Indeed, Silva *et al.* [26] experimentally reported that high temperatures are needed to decompose the hydrides of the $(TiVNb)_{85}Cr_{15}$ alloy. TDS measurements showed that temperatures above 423 K are needed to destabilize the FCC hydride, whereas the BCC intermediate hydride is only destabilized above 523 K.

The calculation of PCT diagrams for the $(TiVNb)_{100-x}Cr_x$ alloys showed that only alloys with Cr content above 30 at.% are likely to be reversible at room temperature. Therefore, in this work we have experimentally investigated the three alloys with high Cr content, namely, $(TiVNb)_{70}Cr_{30}$, $(TiVNb)_{65}Cr_{35}$ and $(TiVNb)_{60}Cr_{40}$. These alloys have been investigated in terms of stable phases and room-temperature hydrogen storage properties. Their PCT curves at 303 K, 323. K, and 343 K have also been experimentally measured and compared with the calculated ones.

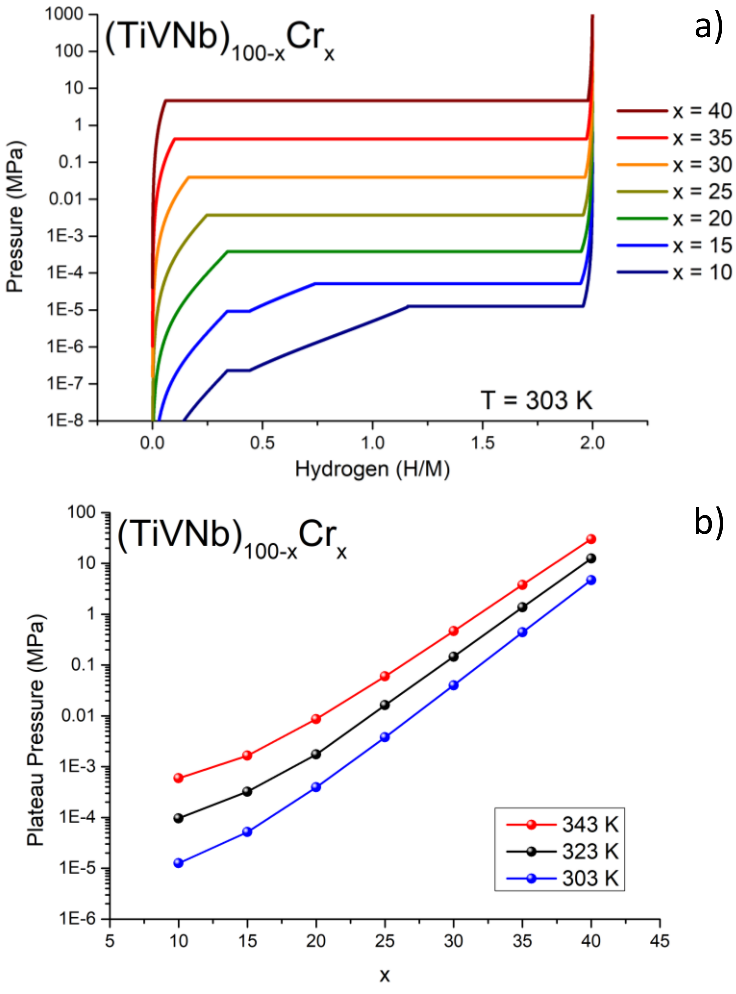

Figure 2: *(a) Calculated PCT curves for the* $(TiVNb)_{100-x}Cr_x$ *alloys at 303 K. (b) Plateau pressure of the* $(TiVNb)_{100-x}Cr_x$ *alloys at 303 K, 323 K, and 343 K. The PCT diagrams of alloys were calculated using the model reported by Zepon et al.* [19].

3.2 Experimental results

3.2.1. Structural Characterization of the as-cast samples

Table 1 presents the experimental chemical composition of the $(TiVNb)_{70}Cr_{30}$, $(TiVNb)_{65}Cr_{35}$, and $(TiVNb)_{60}Cr_{40}$ alloys measured by EDS analysis. For EDS analyses, the as-cast samples were crushed using a steel mortar and pestle. The crushed powders were placed onto a conductive carbon tape in an aluminum sample holder, and EDS measurements of at least 10 powder particles were taken. Figure S1 of the supplementary material file shows a SEM image of the crushed samples. Table 1 presents the average composition of the multiple measurements. One can see that the average compositions for the three alloys are very close to the nominal ones. The standard deviations of the measurements are also presented in Table 1. As it was already reported for other alloys of the Ti-V-Nb-Cr system, solute partitioning takes place during solidification of these alloys, resulting in a dendritic microstructure with a gradient composition [20]. The standard deviation of the EDS measurements is likely to result from the typical segregation of alloying elements during solidification.

Table 1: *Compositional analysis of $(TiVNb)_{100-x}Cr_x$ alloys (x=30, 35 and 40).*

	As-cast chemical composition (at.%)					
	$(TiVNb)_{70}Cr_{30}$		**$(TiVNb)_{65}Cr_{35}$**			**$(TiVNb)_{60}Cr_{40}$**
	Nomin.	**EDS**	**Nomin.**	**EDS**	**Nomin.**	**EDS**
Ti	23.33	25±1	21.66	24.0±4	20	21.9±3
V	23.33	22.8±2	21.66	21.3±2	20	19.8±4
Nb	23.33	22.3±7	21.66	21±1	20	19±1
Cr	30	28.8±4	35	33.7±4	40	38.4±4

Fig. 3 shows the XRD diffraction patterns of the as-cast samples. The XRD pattern of the $(TiVNb)_{70}Cr_{30}$ alloy indicates a single-phase BCC solid solution with the lattice parameter 3.115(2) Å. The $(TiVNb)_{65}Cr_{35}$ alloy is predominantly BCC with the lattice parameter 3.099(1) Å however, its XRD pattern presents low-intensity peaks of the C15 Friauf-Laves phase ($MgCu_2$

type, Fd-3m, 227). A mixture of phases (C15+BCC) was also found for the $(TiVNb)_{60}Cr_{40}$ alloy. The XRD pattern of this alloy suggests a high fraction of the C15 phase (with the lattice parameter 7.039(1) Å) on the expenses of the BCC solid solution. Figure S2 of the Supplementary data file shows the Rietveld refinements for the as-cast alloys. The BCC phase was described considering a random BCC solid solution, in which the atoms occupy the 2a Wyckoff position. The atoms' occupancies were adjusted following the EDS analysis (Table 1). The C15 structure was described as $NbCr_2$ intermetallic with Cr and V (smaller atoms) occupying the same Wyckoff position 16d, while Ti and Nb (biggest atoms) occupied the 8a position. It is worth mentioning that even with good adjustment, a quantitative phase analysis by the Rietveld method could not be performed as the correct composition of each phase could not be determined.

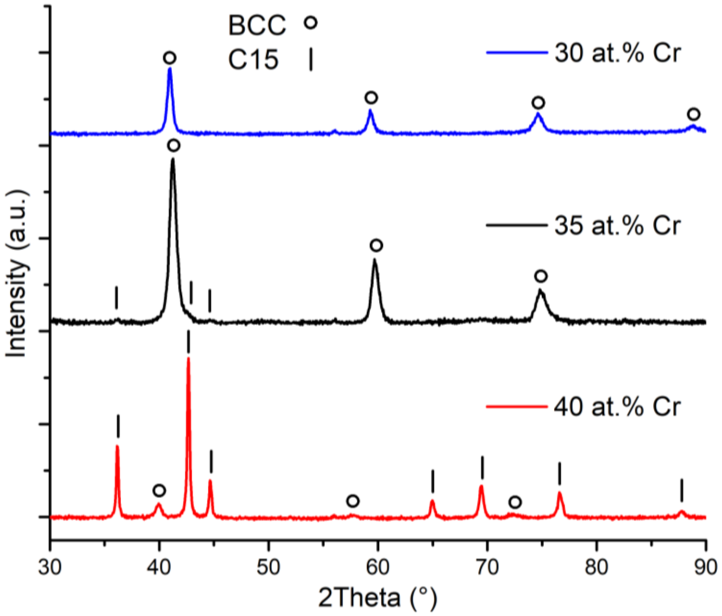

Figure 3: *Indexed XRD patterns of as-cast alloys. The respective compositions are indicated in the figure.*

The XRD results indicate that increasing the Cr concentration induces the formation of C15 Laves phase. According to the CALPHAD calculation (Fig. 1), the precipitation temperature of C15 increases with the increasing of Cr/(TiVNb) ratio. Moreover, solute partitioning during solidification might lead to the formation of the C15 phase at the final stages of solidification. This is more likely to occur at higher Cr contents. Therefore, for the processing route applied in this work, to have a major BCC phase, the Cr content of the $(TiVNb)_{100-x}Cr_x$ system must be limited to approximately 35 at.%. Above this threshold, the fraction of C15 phase increases considerably, as observed experimentally for the $(TiVNb)_{60}Cr_{40}$.

3.2.2 Room-temperature hydrogen absorption kinetics and characterization of the formed hydrides

The kinetic curves for the first hydrogenation of the $(TiVNb)_{70}Cr_{30}$, $(TiVNb)_{65}Cr_{35}$, and $(TiVNb)_{60}Cr_{40}$ alloys under 1.5 MPa at room temperature are presented in Figure 4(a). The three alloys presented fast hydrogenation, reaching maximum capacity in less than two minutes. The $(TiVNb)_{70}Cr_{30}$ alloy absorbs 3.06 wt.%, equivalent to H/M = 1.89. Fig. 4(b) shows the XRD patterns of the hydrides after absorption measurement. One can see that the FCC hydride (a = 4.360(3) Å) was formed for the $(TiVNb)_{70}Cr_{30}$ alloy. It is also possible to see some peaks associated with a hydrogenated BCC phase with increased lattice parameter from 3.115(2) Å for the as-cast sample to 3.22(4) Å after absorption experiment. The Rietveld analysis for XRD patterns collected after hydrogenation are shown in Fig. S3 of the Supplementary material. The $(TiVNb)_{65}Cr_{35}$ alloy achieved a gravimetric capacity of 2.8 wt.% (H/M = 1.7). The XRD analysis for the $(TiVNb)_{65}Cr_{35}$ alloy after absorption measurement presents a major BCC phase with a small fraction of C15 phase. Furthermore, an unknown peak of about 80° can be observed. This peak cannot be indexed as any hydride or initial phase from the as-cast condition. Moreover, as will be further discussed, there is no evidence of a second phase occurring during desorption. Therefore, the authors inferred that it is an experimental artifact. Given the small fraction of C15 phase and its small increase of the lattice parameter, from 7.04(3) Å to 7.08(4) Å for the as-cast alloy and hydrogenated state, respectively, it is possible to infer that most of the hydrogen storage capacity is associated with the hydrogenation of the BCC phase. The lattice parameter of the BCC phase increases from 3.099(1) Å for the initial alloy to 3.188(2) Å after absorption, resulting in a volume increase of 2.64 $Å^3$. According to the well-known Peisl relationship (the volume of an interstitial hydrogen is between 2.0 and 2.9 $Å^3$) [27], such volume expansion should correspond to a hydrogen uptake between 0.45 and 0.66 H/M, significantly lower than the measured capacity of H/M =1.7. Based on the previous results for the $(TiVNb)_{70}Cr_{30}$ alloy and on the thermodynamic calculation presented in section 3.1.2, it is suggested that an FCC hydride was formed during absorption measurement. However, given the high equilibrium plateau pressure between the BCC phase and the FCC hydride, the FCC hydride spontaneously desorbed hydrogen as the system pressure was released. In this case, only the intermediate BCC hydride with H/M ≈ 0.5 can be observed in the XRD pattern.

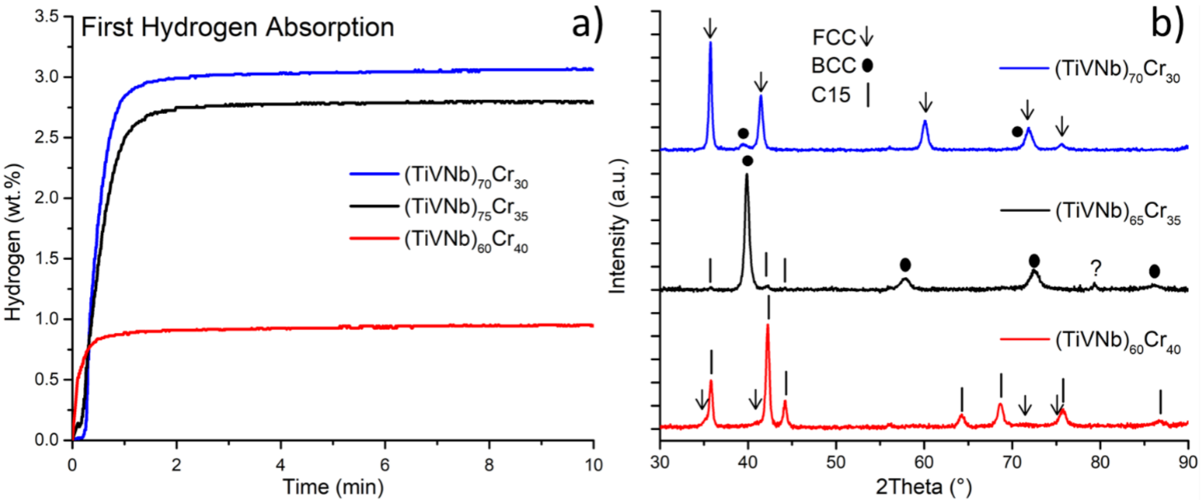

Figure 4: *(a) Hydrogen absorption kinetic curves of the* $(TiVNb)_{70}Cr_{30}$, $(TiVNb)_{65}Cr_{35}$, *and* $(TiVNb)_{60}Cr_{40}$ *alloys, and (b) X-ray diffraction patterns obtained after the first hydrogenation experiment of each studied alloy. Hydrogenation was performed at room temperature and final pressure of 1.5* MPa *of* H_2. *For XRD measurements, a vacuum was performed before removing the sample from the volumetric apparatus.*

The maximum absorption capacity for the $(TiVNb)_{60}Cr_{40}$ alloy was around 0.95 wt.% (Fig. 4(a)), which is significantly lower than the other two BCC alloys. The XRD collected after hydrogenation measurement indicates a major C15 phase with an expanded lattice parameter (7.039(1) Å to 7.10(1) Å), together with a minor amount of an FCC hydride resulted from the hydrogenation of the BCC phase. These results indicate that both phases contribute to the hydrogenation. However, the volume expansion of the C15 phase was 9.2 Å^3, which represents only a H/M between 0.12 and 0.19, indicating a relatively poor hydrogenation. The hydrogenation of C15-based systems has been intensively studied previously. These intermetallics may exhibit good hydrogen storage properties, including good capacity and cyclic stability [28,29]. In these systems, all interstitial sites are tetrahedral, and the hydrogen atoms can occupy the sites coordinated by [A_2B_2], [AB_3] and [B_4] polyhedra [30]. As established by Westlake, the different tetrahedra's occupancy depends significantly on geometrical features [31]. Consequently, the size of the coordination polyhedra and the nature of their constituents are crucial to understand the hydrogen storage behavior of these compounds. Thus, a comprehensive study of the $(TiVNb)_{60}Cr_{40}$ C15-type hydrides demands further investigation, which requires advanced techniques such as, neutron diffraction and nuclear magnetic resonance, that is presently beyond this research's scope.

Fig. 5 (a-c) shows the coupled DSC, TGA and QMS analyses for the three alloys after the first hydrogenation experiment. The DSC analysis of the $(TiVNb)_{70}Cr_{30}$ sample (Fig. 5(a)) indicates three overlapped endothermic peaks with an onset temperature above 480 K for the first peak. These endothermic events are followed by the hydrogen released, evidenced by the QMS signal. The TGA curve indicates three inflection points that agree with the endothermic events. The XRD patterns of the alloys after thermal analysis can be seen in Fig. 6. Their respective Rietveld refinements are shown in Fig. S4. The XRD pattern of the $(TiVNb)_{70}Cr_{30}$ alloy suggests that the sample retrieves the initial BCC structure with lattice parameter of 3.103(5) Å, very close to the initial value. The mass loss determined by TGA was about 3.0 wt.%, in good agreement with the absorbed capacity via kinetic measurements.

The thermal analysis of the $(TiVNb)_{65}Cr_{35}$ sample is displayed in Fig. 5(b). Only a single endothermic event is observed, with on-set temperature of around 600 K. Such endothermic event is accompanied by hydrogen release, as observed in the QMS result, resulting in a mass loss determined by TGA of 0.91 wt.%. As shown in Fig. 6, the XRD pattern after thermal analysis indicates a major BCC phase and small peaks from a minor fraction of C15 phase. After thermal analysis, the BCC lattice parameter decreases to 3.08(1) Å. According to the Peisl relationship, this volume reduction (3.18 $Å^3$) results in a hydrogen release between 0.9 and 1.3 wt.% (H/M between 0.55 and 0.8), close to the mass loss measured by TGA and way below to the absorption capacity of 2.8 wt.% measured for this alloy. This result supports the hypothesis of the spontaneous desorption of the FCC hydride formed during absorption of the $(TiVNb)_{65}Cr_{35}$ sample.

The $(TiVNb)_{60}Cr_{40}$ sample presented two endothermic events related to hydrogen desorption (Fig. 5(c)). The first event has an onset temperature of around 590 K, followed by the second broad peak. The TGA curve indicates a mass loss around 0.82 wt.% and a clear inflection point following the endothermic events, meaning that at least two phases contribute to the hydrogen release. The TGA indicated a slight decrease of the mass even at high temperatures, indicating that the desorption is not complete at 900 K. The final mass loss is in rather good agreement with the measured capacity via the volumetric technique (0.95 wt.%). The XRD after desorption of the (TiVNb)$_{60}$Cr$_{40}$ sample is displayed in Fig. 6. The lattice parameter of the C15 Laves phase is 7.03(1), which is in very good agreement with the value of the initial material.

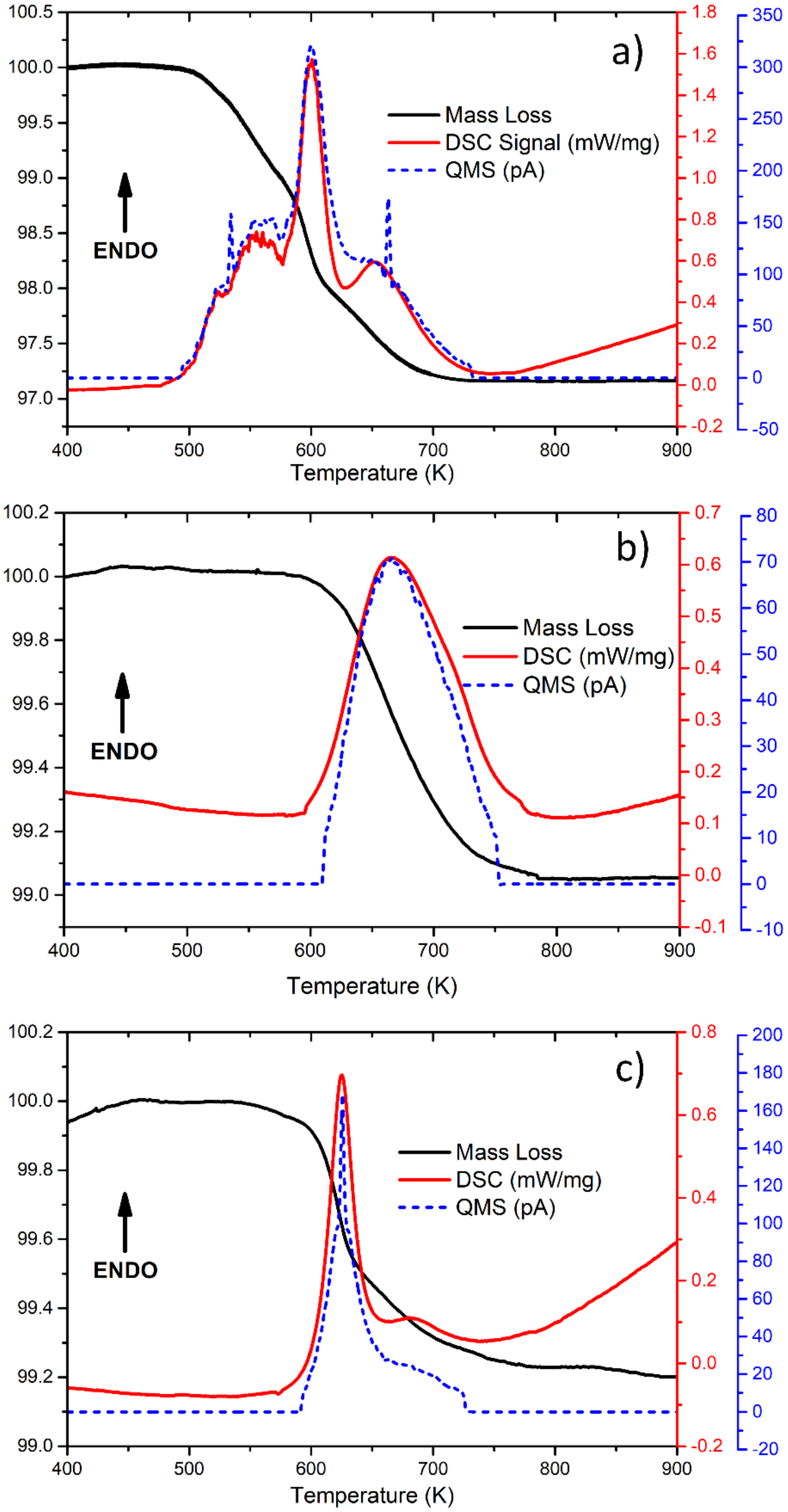

Figure 5: *DSC, TGA and QMS (H_2 signal) curves for (a) $(TiVNb)_{70}Cr_{30}$, (b) $(TiVNb)_{65}Cr_{35}$ and (c) $(TiVNb)_{60}Cr_{40}$ alloys after the first hydrogenation.*

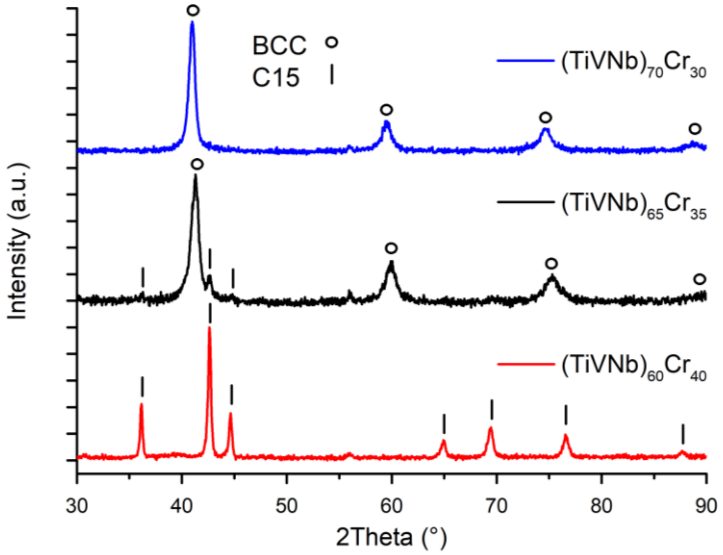

Figure 6: *X-ray diffraction patterns of desorbed samples after thermal analysis. Compositions are indicated in the figure.*

The results presented indicate that increasing the Cr content contributes to the formation of the C15 phase at the expense of the BCC solid solution. While the alloy containing 30 at.% Cr is a single-phase solid solution, further increase of Cr amount to 35 at.% leads to the formation of a small fraction of a secondary C15 phase. However, both alloys absorb hydrogen at room temperature. On the other hand, increasing the Cr content to 40 at.% leads to the formation of a major C15 phase, which has low hydrogen storage capacity. Thus, focusing on the study of BCC alloys, the increase in the Cr content to levels up to 40 at.% is discouraged. Furthermore, the alloys based on the BCC structure showed clear signs of spontaneous desorption at room temperature, which is important for room-temperature cyclability and reversibility. Therefore, the next sessions of this work aim to study the thermodynamics and reversible hydrogen storage capacity of the $(TiVNb)_{70}Cr_{30}$ and $(TiVNb)_{65}Cr_{35}$ alloys, focusing on the effect of Cr content on the thermodynamic, reversibility and cyclability of the BCC alloys.

3.2.3 Experimental PCT diagrams

Fig. 7 (a-b) displays the PCT curves for the $(TiVNb)_{70}Cr_{30}$ and $(TiVNb)_{65}Cr_{35}$ alloys. The PCTs are collected at 303, 323 and 343 K. It is worth mentioning that, for each alloy, the same sample was used for the measurement at the three different temperatures. After each PCT measurement, the samples were exposed to 723 K under a dynamic primary vacuum for 3h. PCT curves of the two alloys displayed low and high plateaus. The first plateau at low equilibrium pressure was below the low-pressure limit of detection of the equipment. Such low equilibrium pressure plateau is related to the equilibrium between the dilute BCC (α-phase) and the BCC intermediate hydride (β-phase) as already reported for the $(TiVNb)_{85}Cr_{15}$ alloy [22,26]. Therefore, differently from the thermodynamic calculation that predicted the formation of only a single plateau for the $(TiVNb)_{70}Cr_{30}$ and $(TiVNb)_{65}Cr_{35}$ alloys, the experimental results showed that increasing the Cr content does not suppress the first plateau pressure.

The second plateau, which refers to the equilibrium between the β phase and the FCC hydride (δ-phase), takes place at higher pressures. A pronounced hysteresis is observed in the PCT curves for the two studied alloys. The hysteresis phenomenon with one order of magnitude difference between the absorption and desorption plateau pressure has been already reported for other multicomponent BCC alloys, including those of the Ti-V-Nb-Cr system [20,22,26]. Even with a substantial hysteresis, the PCTs curves demonstrate that the $(TiVNb)_{70}Cr_{30}$ and $(TiVNb)_{65}Cr_{35}$ alloys can absorb and desorb hydrogen at the experimental conditions. Table 2 summarizes the experimental values of the equilibrium plateau pressure (for the second plateau) for the two alloys. For the $(TiVNb)_{70}Cr_{30}$ alloy, the absorption/desorption plateau pressures are 0.03 MPa / 0.01 MPa, 0.11 MPa / 0.02 MPa, and 0.34 MPa / 0.08 MPa at 303, 323 and 343 K, respectively. The calculated plateau pressures using the thermodynamic model were only slightly higher than the experimental absorption plateau pressures (0.04 MPa; 0.15 MPa; 0.47 MPa, respectively). The experimental absorption/desorption plateau pressures for the $(TiVNb)_{65}Cr_{35}$ alloy at 303, 323 and 343 K are 0.18 MPa / 0.04 MPa, 0.46 MPa / 0.11 MPa, and 1.11 MPa / 0.31 MPa, respectively. In this case, the calculated plateau pressures (0.44 MPa; 1.37 MPa; 3.78 MPa, respectively) were also higher than the experimental ones. Although the predicted plateau pressures were not exact, their order of magnitude as well as the effect of the temperature were quite well described.

Fig. 7(c) displays the van't Hoff plot for the second hydrogenation event obtained from the experimental data. Table 2 presents the comparison between the calculated and experimental enthalpies and entropies for hydrogen absorption and desorption in both alloys. One can see the calculated enthalpies for both alloys are slightly underestimated, which resulted in the higher calculated plateau pressures than the experimental ones. The calculated entropies are slightly underestimated for the $(TiVNb)_{70}Cr_{30}$ alloy and very well predicted for the $(TiVNb)_{65}Cr_{35}$ alloy.

Therefore, the PCT diagram calculation using the model proposed by Zepon et al. [19] is a suitable tool for finding alloy compositions with equilibrium plateau pressures just above atmospheric pressure at low or moderate temperatures. Moreover, the effect of the variation of Cr/(TiVNb) ratio on the thermodynamic properties of the alloys is also reasonably predicted.

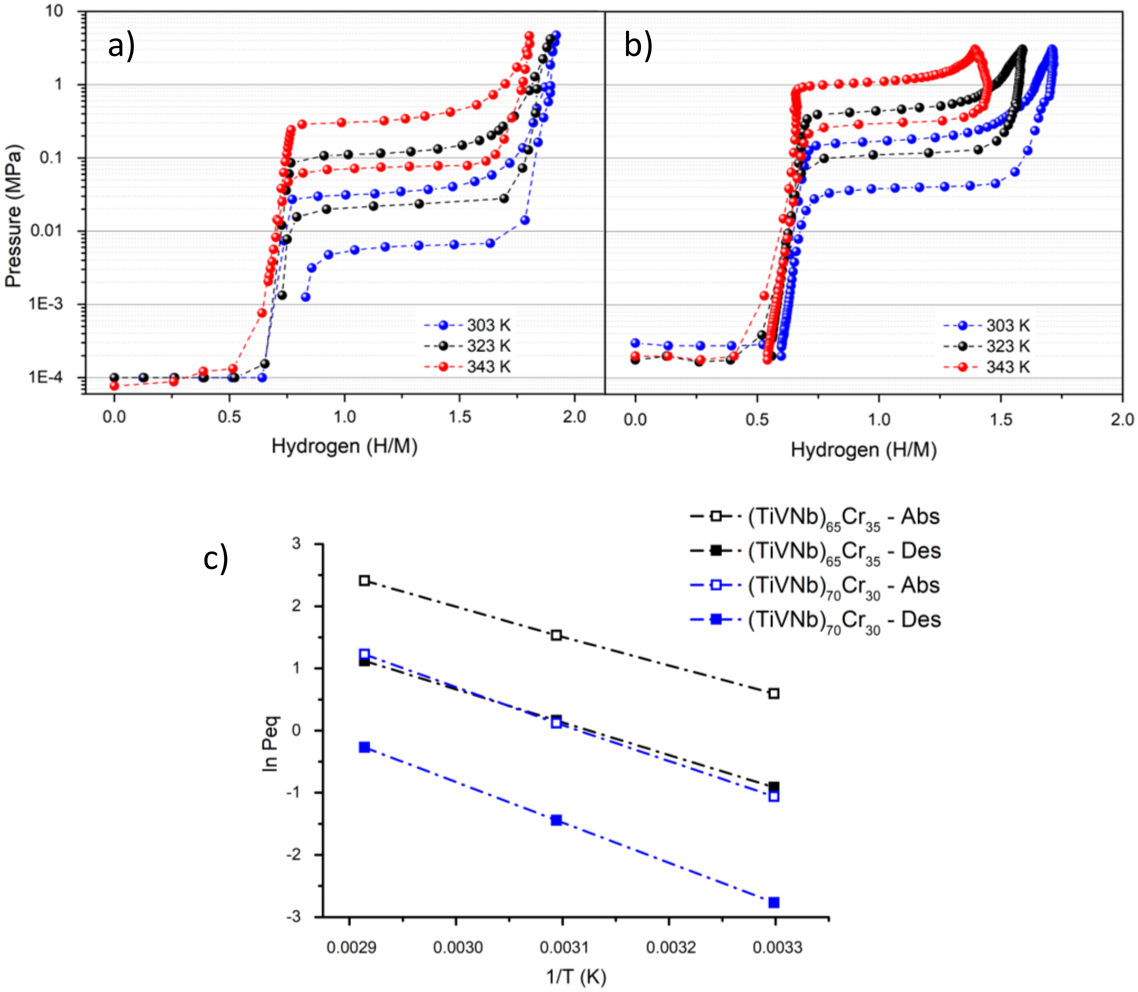

Figure 7: *PCT curves collected at 303, 323 and 343 K for (a) $(TiVNb)_{70}Cr_{30}$; (b) $(TiVNb)_{65}Cr_{35}$. (c) Respective van't Hoff plot for the equilibrium plateau pressures.*

Table 2: *Thermodynamic data from the experimental and calculated PCT curves. Thermodynamic quantities calculated by modeling are represented in absolute values.*

	Plateau Pressures (MPa) 303 K; 323 K; 343 K		**Plateau Enthalpy (kJ/mol H_2)**		**Plateau Entropy (J/K.mol H_2)**	
	Experimental Abs/des	**Calculated**	**Experimental Abs/Des**	**Calculated**	**Experimental Abs/Des**	**Calculated**
(TiVNb)$_{70}$Cr$_{30}$	0.03/0.01; 0.11/0.02; 0.34/0.08	0.04; 0.15; 0.47	-49/+54	43.8	-154/+155	138.9
(TiVNb)$_{75}$Cr$_{35}$	0.18/0.04; 0.46; 0.11; 1.11/0.31	0.44; 1.37; 3.78	-39/+44	37.4	-134/+137	136.7

The very low equilibrium plateau pressure between the α- and β-phases for the (TiVNb)$_{70}$Cr$_{30}$ and (TiVNb)$_{65}$Cr$_{35}$ alloys and the results of DSC analysis (Figure 5), indicating that total desorption can only be achieved at very high temperatures, suggest that the alloys' reversible hydrogen storage capacity results from the second plateau (β ↔ δ), which corresponds to a hydrogen uptake of H/M ≈ 1, *i.e.*, approximately half of the absolute capacity (≈ 2 H/M). This behavior is in fact, typical for classical BCC alloys and is one of the main drawbacks for practical applications of these alloys [32]. Nevertheless, taking advantage of the wide compositional field of MCAs, the proposed approach can be applied to tune the thermodynamics and increase the reversible capacity of BCC-MCAs systems, opening up new avenues for MHs' application.

3.2.4 Room temperature reversibility and cycling performance

The cycling performances were evaluated by measuring the hydrogen absorption capacity during 30 cycles, as shown in Fig. 8(a). In the first cycle, both samples reproduced the absolute capacity from the kinetic measurement (Fig (4a)), achieving capacity of hydrogen uptake around H/M = 2. The hydrogenation was carried at room temperature at a H_2 pressure of 1.5 MPa. Then, the hydride was exposed to dynamic primary vacuum for 10 minutes and again subjected to hydrogenation. In the second cycle the $(TiVNb)_{70}Cr_{30}$ and $(TiVNb)_{65}Cr_{35}$ alloys achieved a hydrogen to metal ratio 0.56 and 0.98, respectively. These results indicate that the settled experimental conditions are enough to decompose the $(TiVNb)_{65}Cr_{35}$ hydride, allowing second hydrogenation related to the $\beta \rightarrow \delta$ transition, which agrees with the thermodynamic results (Fig 7(b)). On the other hand, the low hydrogen uptake of the $(TiVNb)_{70}Cr_{30}$ suggests that the dihydride was not fully desorbed. The plateau pressure of the $(TiVNb)_{70}Cr_{30}$ is around 0.006 MPa at 303 K. Although a primary vacuum pump (0.1 Pa) was used, this level is not necessarily achieved in the sample holder and there is also a delay to achieve high vacuum level. Thus, after the third cycle, the time for dehydrogenation was increased from 10 to 60 minutes. This procedure improved the hydrogen absorption capacity. As shown in Fig. 8(a), in the fourth cycle, the sample absorbed a $H/M \approx 1.13$, which was reproduced in the subsequent cycles.

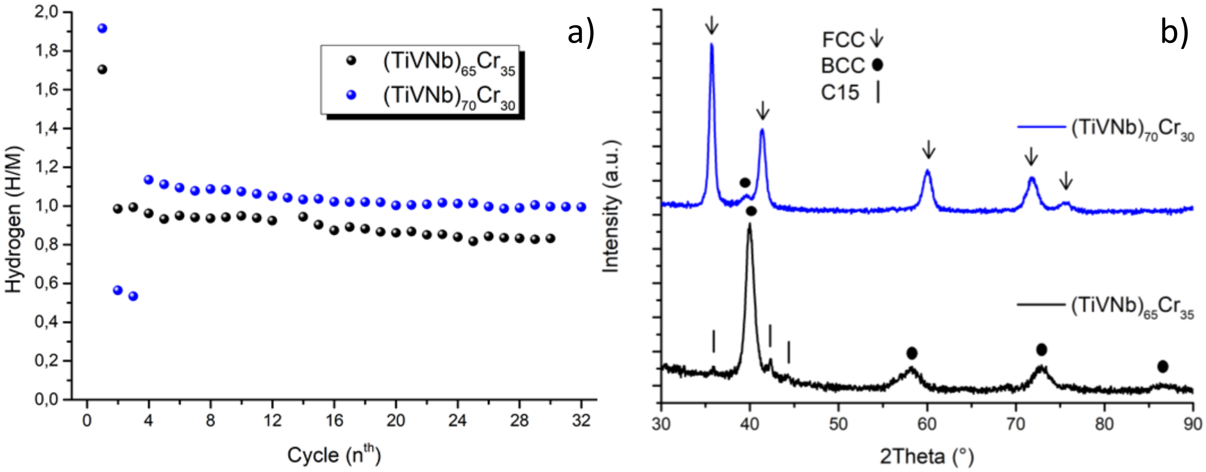

Figure 8: *(a) Reversible hydrogen absorption capacity at RT (b) XRD patterns of as absorbed samples after the cycling experiment. It is significant to mention that this analysis was carried out after the 30th cycle, and a line vacuum was done before taking the sample out from the volumetric apparatus.*

The cycling experiments showed a slight reduction in the reversible capacity along the cycles, from 1.13 to 0.99 H/M for $(TiVNb)_{70}Cr_{30}$ alloy and from 0.98 to 0.83 H/M for the $(TiVNb)_{65}Cr_{35}$ MCA. It is worth mentioning that for the $(TiVNb)_{70}Cr_{30}$ alloy, the 4th and 32nd cycles were considered for comparison. Figure 8(b) shows the XRD patterns collected after the 30th absorption cycle. Again, a major FCC hydride with a minor fraction of BCC hydride was observed for the $(TiVNb)_{70}Cr_{30}$ alloy. For the $(TiVNb)_{65}Cr_{35}$ alloy, the major BCC hydride phase with small fraction of C15 phase is observed. Therefore, the XRD patterns for the alloys after the 30th absorption cycle are quite similar to those measured after first absorption (Fig. 4(b)). The slight reduction of capacity after cycling might be related to the increase in the defect's concentration over the cycles. It has been reported that the crystal lattice defects and micro-strains diminish the reversible hydrogen storage capacity of multicomponent BCC alloys [22,33]. This deleterious behavior comes from modifications on the local lattice structure. According to Wang *et al.* [33], it is a consequence of a trap effect, where the lattice defects retain the hydrogen atoms. Since the samples were cycled at room temperature, the influence of the defects on the reversible capacity could become even more important because thermal processes that contribute to the relaxation of the crystal structure are not activated. However, the reduction of reversible capacity after 30 cycles was quite small for both samples, indicating excellent cycling stability of these alloys.

4. Conclusions

The $(TiVNb)_{100-x}Cr_x$ system was investigated. A wide compositional range was previously assessed via a combination of two design strategies: (i) the CALPHAD approach was applied to predict fields of interest to obtain BCC alloys; (ii) a thermodynamic modeling to calculate PCT diagrams to estimate the equilibrium plateau for alloys with different Cr/(TiVNb) ratios. The $(TiVNb)_{100-x}Cr_x$ with x = 30, 35 and 40 alloys were selected and produced by arc-melting and characterized via a combination of structural, thermal, and volumetric techniques. The results were interpreted, and the following conclusions are made:

- The microstructures of the $(TiVNb)_{30}Cr_{70}$ and $(TiVNb)_{65}Cr_{35}$ alloys produced by arc-melting were composed of a major BCC phase, as predicted by CALPHAD calculation. The $(TiVNb)_{30}Cr_{70}$ and $(TiVNb)_{65}Cr_{35}$ alloys absorbed hydrogen with very fast kinetics at room temperature by forming FCC hydrides with H/M ≈ 2. Their total hydrogen storage capacities were 3.1 wt.% and 2.8 wt.%, respectively.
- Increasing the Cr content to 40 at.% leads to the formation of a high fraction of C15 Friauf-Laves phase at the expense of the BCC solid solution. This behavior was well described by

thermodynamic calculation carried out by the CALPHAD. The C15 phase does not absorb a significant amount of hydrogen, decreasing the alloy's gravimetric capacity.

- The equilibrium plateau pressure between the BCC and FCC hydrides increases as the Cr content increases, resulting in less stable MHs. Thus, the $(TiVNb)_{70}Cr_{30}$ and $(TiVNb)_{65}Cr_{35}$ alloys showed a reversible hydrogen capacity of H/M ≈ 1 at near room-temperature.
- The cycling stability of the $(TiVNb)_{30}Cr_{70}$ and $(TiVNb)_{65}Cr_{35}$ alloys indicates that the hydrogen uptake slightly decreases over the cycles, which could be associated with increasing lattice defects that might act as trapping sites for hydrogen.

Acknowledgments

This work was financially supported in part by the Serrapilheira Institute (grant number Serra-1709-17362), in part by the CAPES-COFECUB cooperation program (process number 88887.627737/2021-00, project number 88887.191910/2018-00), in part by the São Paulo Research Foundation – FAPESP (process number 2020/07707-6), and in part by the Brazilian National Council for Scientific and Technological Development – CNPq (Grant number: 309467/2021-7). This study was financed in part by the Coordenação de Aperfeiçoamento de Pessoal de Nível Superior - Brasil (CAPES) - Finance Code 001.

5. References

[1] M. Hirscher, V.A. Yartys, M. Baricco, J. Bellosta von Colbe, D. Blanchard, R.C. Bowman, D.P. Broom, C.E. Buckley, F. Chang, P. Chen, Y.W. Cho, J.C. Crivello, F. Cuevas, W.I.F. David, P.E. de Jongh, R. V Denys, M. Dornheim, M. Felderhoff, Y. Filinchuk, G.E. Froudakis, D.M. Grant, E.M.A. Gray, B.C. Hauback, T. He, T.D. Humphries, T.R. Jensen, S. Kim, Y. Kojima, M. Latroche, H.W. Li, M. V Lototskyy, J.W. Makepeace, K.T. Møller, L. Naheed, P. Ngene, D. Noréus, M.M. Nygård, S. ichi Orimo, M. Paskevicius, L. Pasquini, D.B. Ravnsbæk, M. Veronica Sofianos, T.J. Udovic, T. Vegge, G.S. Walker, C.J. Webb, C. Weidenthaler, C. Zlotea, Materials for hydrogen-based energy storage – past, recent progress and future outlook, J. Alloys Compd. 827 (2020) 153548. doi:10.1016/j.jallcom.2019.153548.

[2] D.B. Miracle, O.N. Senkov, A critical review of high entropy alloys and related concepts, Acta Mater. 122 (2017) 448–511. doi:10.1016/j.actamat.2016.08.081.

[3] F. Marques, M. Balcerzak, F. Winkelmann, G. Zepon, M. Felderhoff, Environmental Science, Green Technol. An A-to-Z Guid. (2021). doi:10.4135/9781412975704.n47.

[4] Y.-F. Kao, S.-K. Chen, J.-H. Sheu, J.-T. Lin, W.-E. Lin, J.-W. Yeh, S.-J. Lin, T.-H. Liou, C.-W. Wang, Hydrogen storage properties of multi-principal-component CoFeMnTixVyZrz alloys, Int. J. Hydrogen Energy. 35 (2010) 9046–9059. doi:10.1016/j.ijhydene.2010.06.012.

[5] Z. Li, Y. Yan, H. Huang, B. Liu, Y. Lv, B. Zhang, W. Lv, J. Yuan, Y. Wu, Effects of the different element substitution on hydrogen storage properties of Ti0.8Zr0.2Mn0.9Cr0.6V0.3M0.2 (M = Fe, Ni, Co), J. Alloys Compd. 908 (2022) 164605. doi:10.1016/j.jallcom.2022.164605.

[6] V., B. Sarac, E. Berdonosova, T. Karazehir, A. Lassnig, C. Gammer, M. Zadorozhnyy, S. Ketov, S. Klyamkin, J. Eckert, Evaluation of hydrogen storage performance of ZrTiVNiCrFe in electrochemical and gas-solid reactions, Int. J. Hydrogen Energy. 45 (2020) 5347–5355. doi:10.1016/j.ijhydene.2019.06.157.

[7] B. Sarac, V. Zadorozhnyy, Y.P. Ivanov, F. Spieckermann, S. Klyamkin, E. Berdonosova, M. Serov, S. Kaloshkin, A.L. Greer, A.S. Sarac, J. Eckert, Transition metal-based high entropy alloy microfiber electrodes: Corrosion behavior and hydrogen activity, Corros. Sci. 193 (2021) 109880. doi:10.1016/j.corsci.2021.109880.

[8] J. Chen, Z. Li, H. Huang, Y. Lv, B. Liu, Y. Li, Y. Wu, J. Yuan, Y. Wang, Superior cycle life of TiZrFeMnCrV high entropy alloy for hydrogen storage, Scr. Mater. 212 (2022) 114548. doi:10.1016/j.scriptamat.2022.114548.

[9] P. Edalati, R. Floriano, A. Mohammadi, Y. Li, G. Zepon, H.W. Li, K. Edalati, Reversible room temperature hydrogen storage in high-entropy alloy TiZrCrMnFeNi, Scr. Mater. 178 (2020) 387–390. doi:10.1016/j.scriptamat.2019.12.009.

[10] F. Yang, J. Wang, Y. Zhang, Z. Wu, Z. Zhang, F. Zhao, J. Huot, J. Grobivć Novaković, N. Novaković, Recent progress on the development of high entropy alloys (HEAs) for solid hydrogen storage: A review, Int. J. Hydrogen Energy. 47 (2022) 11236–11249. doi:10.1016/j.ijhydene.2022.01.141.

[11] R.B. Strozi, D.R. Leiva, J. Huot, W.J. Botta, G. Zepon, An approach to design single BCC

Mg-containing high entropy alloys for hydrogen storage applications, Int. J. Hydrogen Energy. 46 (2021) 25555–25561. doi:10.1016/j.ijhydene.2021.05.087.

[12] N. Pineda-Romero, M. Witman, V. Stavila, C. Zlotea, The effect of 10 at.% Al addition on the hydrogen storage properties of the Ti0.33V0.33Nb0.33 multi-principal element alloy, Intermetallics. 146 (2022) 107590. doi:10.1016/j.intermet.2022.107590.

[13] C. Zlotea, M.A. Sow, G. Ek, J.P. Couzinié, L. Perrière, I. Guillot, J. Bourgon, K.T. Møller, T.R. Jensen, E. Akiba, M. Sahlberg, Hydrogen sorption in TiZrNbHfTa high entropy alloy, J. Alloys Compd. 775 (2019) 667–674. doi:10.1016/j.jallcom.2018.10.108.

[14] S. Miraglia, D. Fruchart, N. Skryabina, M. Shelyapina, B. Ouladiaf, E.K. Hlil, P. De Rango, J. Charbonnier, Hydrogen-induced structural transformation in TiV0.8Cr1.2 studied by in situ neutron diffraction, J. Alloys Compd. 442 (2007) 49–54. doi:10.1016/j.jallcom.2006.10.168.

[15] Y. Fukai, The Metal–Hydrogen System Basic Bulk Properties, in: 1990: p. 608. doi:10.1007/978-1-4899-6826-5.

[16] A. Mohammadi, Y. Ikeda, P. Edalati, M. Mito, B. Grabowski, H.-W. Li, K. Edalati, High-Entropy Hydrides for Fast and Reversible Hydrogen Storage at Room Temperature: Binding-Energy Engineering via First-Principles Calculations and Experiments, Acta Mater. 236 (2022) 118117. doi:10.1016/j.actamat.2022.118117.

[17] V. Zadorozhnyy, I. Tomilin, E. Berdonosova, C. Gammer, M. Zadorozhnyy, I. Savvotin, I. Shchetinin, M. Zheleznyi, A. Novikov, A. Bazlov, M. Serov, G. Milovzorov, A. Korol, H. Kato, J. Eckert, S. Kaloshkin, S. Klyamkin, Composition design, synthesis and hydrogen storage ability of multi-principal-component alloy TiVZrNbTa, J. Alloys Compd. 901 (2022) 163638. doi:10.1016/j.jallcom.2022.163638.

[18] M.M. Nygård, G. Ek, D. Karlsson, M.H. Sørby, M. Sahlberg, B.C. Hauback, Counting electrons - a new approach to tailor the hydrogen sorption properties of high-entropy alloys, Acta Mater. 175 (2019) 121–129. doi:10.1016/j.actamat.2019.06.002.

[19] G. Zepon, B.H. Silva, C. Zlotea, W.J. Botta, Y. Champion, Thermodynamic modelling of hydrogen-multicomponent alloy systems: Calculating pressure-composition-temperature diagrams, Acta Mater. 215 (2021) 117070. doi:10.1016/j.actamat.2021.117070.

[20] R.B. Strozi, D.R. Leiva, G. Zepon, W.J. Botta, J. Huot, Effects of the Chromium Content in (TiVNb)100−xCrx Body-Centered Cubic High Entropy Alloys Designed for Hydrogen

Storage Applications, Energies. 14 (2021) 3068. doi:10.3390/en14113068.

[21] B.H. Toby, R.B. Von Dreele, GSAS-II: The genesis of a modern open-source all purpose crystallography software package, J. Appl. Crystallogr. 46 (2013) 544–549. doi:10.1107/S0021889813003531.

[22] B.H. Silva, C. Zlotea, Y. Champion, W.J. Botta, G. Zepon, Design of TiVNb-(Cr, Ni or Co) multicomponent alloys with the same valence electron concentration for hydrogen storage, J. Alloys Compd. 865 (2021) 158767. doi:10.1016/j.jallcom.2021.158767.

[23] T.B. Flanagan, W.A. Oates, Some thermodynamic aspects of metal hydrogen systems, 406 (2005) 16–23. doi:10.1016/j.jallcom.2004.11.108.

[24] J. Garcés, The configurational entropy of mixing of interstitials solid solutions, Appl. Phys. Lett. 96 (2010). doi:10.1063/1.3400221.

[25] O.A. Pedroso, W.J. Botta, G. Zepon, An open-source code to calculate pressure-composition-temperature diagrams of multicomponent alloys for hydrogen storage, Int. J. Hydrogen Energy. (2022). doi:10.1016/j.ijhydene.2022.07.179.

[26] B.H. Silva, C. Zlotea, G. Vaughan, Y. Champion, W.J. Botta, G. Zepon, Hydrogen absorption/desorption reactions of the (TiVNb)85Cr15 multicomponent alloy, J. Alloys Compd. 901 (2022) 163620. doi:10.1016/j.jallcom.2022.163620.

[27] H. Peisl, Lattice strains due to hydrogen in metals, in: G. Alefeld, J. Völkl (Eds.), Hydrog. Met. I. Top. Appl. Physics. Vol 28, Springer, Berlin, Heidelberg, 1978: pp. 53–74. doi:10.1007/3540087052_42.

[28] I.D. Wijayanti, R. Denys, Suwarno, A.A. Volodin, M. V. Lototskyy, M.N. Guzik, J. Nei, K. Young, H.J. Roven, V. Yartys, Hydrides of Laves type Ti–Zr alloys with enhanced H storage capacity as advanced metal hydride battery anodes, J. Alloys Compd. 828 (2020) 154354. doi:10.1016/j.jallcom.2020.154354.

[29] A. Hariyadi, S. Suwarno, R. V. Denys, J.B. von Colbe, T.O. Sætre, V. Yartys, Modeling of the hydrogen sorption kinetics in an AB2 laves type metal hydride alloy, J. Alloys Compd. 893 (2022) 162135. doi:10.1016/j.jallcom.2021.162135.

[30] A. V. Skripov, Hydrogen jump motion in Laves-phase hydrides: Two frequency scales, J. Alloys Compd. 404–406 (2005) 224–229. doi:10.1016/j.jallcom.2004.12.160.

[31] D.G. Westlake, Site occupancies and stoichiometries in hydrides of intermetallic compounds: Geometric considerations, J. Less-Common Met. 90 (1983) 251–273.

doi:10.1016/0022-5088(83)90075-9.

[32] J. Huot, Metal Hydrides, in: M. Hirscher (Ed.), Handb. Hydrog. Storage New Mater. Futur. Energy Storage, Wiley-VCH Verlag GmbH & Co. KGaA, 2010: pp. 81–116. doi:10.1002/9783527629800.

[33] Q. Wang, X. Dai, C. Wu, Y. Mao, Y. Chen, X. Cao, Y. Yan, Y. Wang, H. Zhang, Lattice defects and micro-strains in V60Ti25Cr3Fe12 alloy and influence on the ab/desorption of hydrogen, J. Alloys Compd. 830 (2020) 154675. doi:10.1016/j.jallcom.2020.154675.